NASA-CR-202655

A Final Report
NASA Grant No. NCC-1-197
August 1, 1994 - October 31, 1996

NEW CONCENTRIC ELECTRODE METAL-SEMICONDUCTOR-METAL PHOTODETECTORS

Submitted to:

Dr. James McAdoo, MS 468
National Aeronautics and Space Administration
Langley Research Administration
Hampton, VA 23681-0001

Submitted by:

E. Towe
Associate Professor

SEAS Report No. UVA/528503/EE97/101
November 1996

DEPARTMENT OF ELECTRICAL ENGINEERING
UNIVERSITY OF VIRGINIA
SCHOOL OF ENGINEERING AND APPLIED SCIENCE
THORNTON HALL
CHARLOTTESVILLE, VA 22903-2442

SCHOOL OF
ENGINEERING
& APPLIED SCIENCE

University of Virginia
Thornton Hall
Charlottesville, VA 22903

New Concentric Electrode Metal-Semiconductor-Metal Photodetectors

Elias Towe

Department of Electrical Engineering

University of Virginia

Charlottesville, Virginia 22903-2442

(November 19, 1996)

Abstract

A new metal-semiconductor-metal (MSM) photodetector geometry is proposed. The new device has concentric metal electrodes which exhibit a high degree of symmetry and a design flexibility absent in the conventional MSM device. The concentric electrodes are biased to alternating potentials as in the conventional interdigitated device. Because of the high symmetry configuration, however, the new device also has a lower effective capacitance. This device and the conventional MSM structure are analyzed within a common theoretical framework which allows for the comparison of the important performance characteristics.

1. Introduction

Metal-semiconductor-metal (MSM) photodetectors have a potentially important role to play in optoelectronic device integration because of several distinct advantages. Of all the semiconductor photodetectors that have been studied, these devices are the simplest to fabricate. Furthermore, their fabrication technology is fully compatible with that of FETs. This coincidence makes the MSM photodetector an ideal device for optoelectronic integration. Another major advantage of these devices is their superior performance at high frequencies. The desirable high frequency characteristics are partly a consequence of the inherently low capacitances exhibited by the devices. In general, they have lower capacitances per unit area than any of the doped-junction devices. Because of their planar structure, the intrinsic response times of most MSM devices are often limited primarily by the transit time between electrodes. GaAs MSM devices with performance bandwidths in excess of 400 GHz, and Silicon-based devices with bandwidths of up to 30 GHz have been reported [1]. These figures far exceed those reported for any other photodetector structure, including PIN photodiodes. It is also predicted theoretically that devices with bandwidths above 1 THz are possible, albeit with sub-micron feature sizes [2].

1.1. Motivation for Concentric Electrode MSM Photodetectors

Current MSM photodetectors are fabricated with the interdigitated electrode structure shown in Fig. 1. Electronic carriers photogenerated between the electrode gaps are transported to the electrodes primarily by drift along the strong electric field lines established by the bias voltage, thus leading to a signal current. The planar geometry of the MSM device endows it with distinct advantages as a photodetector. In the ideal analysis of a device such as this, one generally assumes that the electrodes extend to infinity in each direction.

Under this assumption, a two-dimensional analysis can be employed to calculate the theoretical performance limits of the device [3]. Real devices, however, have electrodes with finite lengths. One consequence of this is non-idealities which degrade the performance of the practical devices. In particular, the sharp corners associated with the abrupt termination of the electrode fingers and the additional ohmic metallization required for biasing the electrodes cause "crowding" of the electric field lines near the ends of the electrodes. This situation can lead to higher electric field strengths in these regions than what is predicted by the simple two-dimensional consideration. The concomitant disadvantages of the high electric fields are a reduced breakdown voltage and higher capacitance.

We are proposing a way of minimizing these effects by changing the geometry of the device. The proposed new device structure has concentric electrodes which are biased to alternating potentials as in the conventional interdigitated electrode structure. A schematic representation of the new device is shown in Fig. 2. In this configuration, the non-ideal "crowding" of electric field lines associated with the abrupt termination of the electrodes in the interdigitated electrode device structure is minimized. It is anticipated that this device will exhibit superior performance characteristics compared to those of the rectangular interdigitated device. We are in the process of fabricating such devices and the experimental results will be reported elsewhere.

The new MSM photodetector affords one an additional degree of design freedom absent in the conventional detectors. This design freedom is represented by the central disk shown in Fig. 2. This disk is also there because of a necessity; if it were absent, carriers generated in this region would encounter weak electric fields and would be transported to the nearest electrode primarily by diffusion. This would lead to a degradation of the temporal response of the device.

Before continuing, we establish in Fig. 3 the nomenclature to be used in the rest of the

paper. The parameter a denotes an electrode width in both the conventional interdigitated and concentric electrode devices; b is the electrode period in either geometry. In Fig. 3, R_c is the radius of the central disk. The number of annular electrodes is to be represented by N_e. The total number of electrodes, including the central disk, is therefore $N_e + 1$.

2. Methods of Analysis

2.1. General Considerations

Our primary goal in this Section is to establish a framework within which we can analyze both the new concentric electrode device and the conventional interdigitated electrode device. This will enable us to compare the operating characteristics of the devices. In formulating the analysis, we have striven to use methods which are as simple as possible without compromising the accuracy of the results. Rigorous analyses with sophisticated numerical techniques are possible, but such techniques are often computationally complex and extremely time consuming. In some cases they may even obscure the basic physical premise of the analysis.

In order to ensure that our simple models faithfully describe the physical devices, we have also used the numerical solutions of the general, fully coupled drift-diffusion equations for semiconductors to verify the models. We find that our model calculations agree reasonably well with the solutions obtained from the drift-diffusion equations in all cases. Thus, our models are valid to the extent that the drift-diffusion equations adequately describe the physical reality of these devices. In these calculations, we have chosen not to consider hot-electron effects or devices with feature sizes less than 0.5 μm. Such cases are, of course, important, but this is a topic for future studies. Stated below, for the sake of completeness, are the semiconductor drift-diffusion equations appropriate for our analysis. These equations are:

$$\frac{\partial n}{\partial t} = G_n - R_n + \frac{1}{q}\nabla \cdot \mathbf{J}_n \tag{1}$$

$$\frac{\partial p}{\partial t} = G_p - R_p - \frac{1}{q}\nabla \cdot \mathbf{J}_p \tag{2}$$

$$\nabla^2 \varphi = -\frac{q}{\epsilon}(p - n + N_D^+ - N_A^-) \tag{3}$$

$$\mathbf{J}_n = q(n\mu_n \nabla\varphi + D_n \nabla n) \tag{4}$$

$$\mathbf{J}_p = q(p\mu_p \nabla\varphi - D_p \nabla p), \tag{5}$$

where n and p are the electron and hole concentrations, μ_n and μ_p are the field dependent mobilities for electrons and holes, D_n and D_p are the diffusivities of electrons and holes, N_D^+ and N_A^- are the ionized donor and acceptor concentrations, $\mathbf{J}_n$ and $\mathbf{J}_p$ are the electron and hole current densities, ϵ is the dielectric constant for the active semiconductor, and φ is the electrostatic potential. G_n, G_p , R_n, and R_p are the generation and recombination rates for electrons and holes, including optical and thermal generation and Shockley-Read-Hall recombination. The effects of charge traps are considered to be negligible. The numerical solutions to these equations are used to check the accuracy of our models.

2.2. Discussion of the Model Assumptions

In considering the MSM photodetectors in both geometries, a number of simplifying assumptions can be made. First, the active semiconductor layer is assumed to be infinitely thick and uniformly doped. The infinite thickness assumption can be justified on the basis of the absorption depth of the radiation. The issue of the doping uniformity can generally be guaranteed by fabricating the device from material grown by any of the advanced modern crystal growth techniques. The second main assumption is that the devices are operated at a bias point where the semiconductor is fully depleted between the electrodes. The results

reported here are valid only for bias voltages satisfying this condition. In any event, most real MSM devices are operated under this condition if they are intended to function as efficient photodetectors. If an MSM device is not biased to full depletion, the photogenerated carriers are not likely to be fully collected; the carrier transit time and consequently the external optical response will therefore be compromised.

In the calculation of the dark current, it is assumed that the electrodes form ideal Schottky contacts. Furthermore, the effect of image-force lowering of the Schottky barrier height is neglected; this assumption is verified by the full drift-diffusion simulations. Thermionic emission theory has also been taken into account in the determination of the dark current density at the Schottky barriers. This is consistent with the moderate doping levels found in typical MSM photodetectors [4].

If the MSM device is taken to consist of ideal electrodes on top of a perfect dielectric material, then the depletion capacitance associated with the active semiconductor layer can be neglected. This is true for low doping densities and for the typical electrode spacing of most MSM photodetectors and is consistent with other analyses of these devices in the past[3]. Experimental results have shown that these assumptions are fairly reasonable [5].

In the photocurrent considerations, it will be assumed that all the incident photons not reflected at the surface of the device, are absorbed in the depletion region formed around the electrodes. Since the electric field strengths in these regions are generally large, it follows that the generated electron-hole pairs are separated immediately, and it can be assumed that recombination is negligible. This is generally true because the condition $pn \ll n_i^2(T)$ is satisfied in this region.

It is implicit in this discussion that ballistic and velocity overshoot effects are not important; the carriers are assumed to travel with their equilibrium saturated velocity values. This assumption imposes a lower limit to the feature size which can be accurately modeled

within this framework. As stated earlier, we have only considered feature sizes of 0.5 μm and larger.

2.3. Resulting Equations and Methods of Solution

2.3.1. Dark Current

Our development of the dark current relations for both interdigitated and concentric electrode MSM photodetectors will parallel the discussion given by Sze *et al.* for BARITT type devices [6] made by sandwiching a slice of semiconductor material between two metal electrodes. In this work, however, the dark current relation will be derived as a piecewise continuous function over three regions—-exclusive of avalanche breakdown, which we do not consider. The boundaries between these regions are characterized by two bias points. The first is the so-called reach-through voltage, denoted by V_{RT}, which is the bias voltage at which the depletion regions associated with each electrode first touch and the inter-electrode gaps are considered fully depleted. The second point is the flat-band voltage, V_{FB}, which occurs when the slope of the energy bands at the positively biased electrode becomes zero.

The model presented by Sze was developed for one-dimensional, rather than planar MSM devices. To a first order approximation, the behavior of the planar devices can also be analyzed within the one-dimensional framework as long as the dark current flows along a path which is nearly parallel to the plane of the electrodes over much of the device. As can be seen from Fig. 4, which shows dark current vectors generated from a numerical solution of the complete drift-diffusion equations, the current initially flows out of the electrodes in a direction normal to the device surface, but then quickly "bends" to follow a path which is nearly parallel to the plane of the electrodes. This is as it should be because the carriers which constitute the dark current follow the electric field lines, which are nearly parallel to

the plane of the electrodes.

The detailed analysis of our devices, however, can in some instances differ from Sze's in that for the planar MSM devices, surface recombination may play a part in determining the dark current; this is not a factor in the one-dimensional structures. In the discussion here, however, we shall limit ourselves to the cases where surface recombination is negligible. It should be noted that whereas it is possible in the one-dimensional case to derive simple closed-form expressions for the reach-through and the flat-band voltages, in the planar geometry devices, it is a non-trivial task to determine such expressions. These points can, however, be determined by examining the solutions obtained from drift-diffusion simulations. The considerations which lead to the model equations are discussed below.

In accounting for the dark current, we will consider contributions from both carrier types. As an example, we will consider an n-type semiconductor in which electrons are the majority carriers and holes the minority carriers. A similar analysis with holes as the majority carriers (for p-type material) can be easily performed. For the majority carrier dark current, we shall model a pair of electrodes as two back-to-back Schottky diodes and relate the dark current generated in such a structure by the equations

$$I_{n1} = J_{sn} A_1 \left[\exp(V_1/V_t) - 1\right] \tag{6}$$

and

$$I_{n2} = J_{sn} A_2 \left[1 - \exp(-V_2/V_t)\right]. \tag{7}$$

The currents I_{n1} and I_{n2} are the electron dark currents from electrode 1 and 2. The subscript 1 refers to the positively biased electrode while 2 refers to the negatively biased one. The total bias voltage which is dropped across the two electrodes that form the Schottky diodes is

$$V_b = V_1 + V_2. \tag{8}$$

The positive and negative electrode areas are given, respectively, by A_1 and A_2. The thermionic emission current density for electrons from the Schottky electrodes is given by

$$J_{sn} = A_n^* T^2 \exp(-\phi_n / V_t), \tag{9}$$

where A_n^* is the effective Richardson constant for electrons and ϕ_n is the Schottky barrier height for electrons; T is the temperature and $V_t = kT/q$ is the usual thermal voltage. A continuity condition for the dark current from each electrode requires that

$$I_{n1} = I_{n2}. \tag{10}$$

For bias voltages less than the reach-through voltage, V_{RT}, one can solve for the majority carrier dark current as a function of the bias. It is a straight-forward exercise in algebra to show from Eqns. (6) through (10) that the majority carrier dark current is given by

$$I_n = J_{sn} \mathcal{A}_2 \left[\frac{1 - \exp(-V_b/V_t)}{1 + \alpha \exp(-V_b/V_t)} \right], \tag{11}$$

for

$$0 \leq V_b < V_{BR}. \tag{12}$$

This expression has been generalized to the multiple electrode pair case. The total area of the reverse-biased electrodes is denoted by $\mathcal{A}_2$, and $\alpha = \mathcal{A}_2/\mathcal{A}_1$ where $\mathcal{A}_1$ is the corresponding total area of the forward-biased electrodes. Note that the dark current approaches zero as the bias voltage is reduced to zero and it saturates at the value of

$$I_n = J_{sn} \mathcal{A}_2 \tag{13}$$

for values of V_b larger than V_t and for V_b less than the breakdown voltage.

The determination of the minority carrier dark current is fairly lengthy and involved. This current must be evaluated for three different ranges of operating voltages; these are: (i)

voltages less than the reach-through voltage, V_{RT}, (ii) voltages between the reach-through voltage and the flat-band voltage, and (iii) voltages greater than the flat-band voltage but less than the breakdown voltage. For bias voltages less than the reach-through voltage, regions depleted of majority carriers form around each electrode. These regions do not merge. Between the electrodes, in the undepleted regions, the minority carrier dark current must flow by diffusion. The net terminal hole current is therefore the total injected hole current at the the forward-biased electrode minus the hole current lost to recombination in the undepleted regions between the electrodes.

To quantitatively determine the net hole dark current requires the solution of the diffusion equation with the appropriate boundary conditions for the rather complicated geometries presented here. Rather than pursuing this method of solution, we will determine the upper bound of the magnitude of the hole dark current and compare it to the electron dark current. If it is comparable to or larger than the electron dark current, then a full solution of the diffusion equation would be necessary and justified.

At the forward-biased electrode, the thermionically emitted hole current is given by

$$I_{p1} = A_p^* \mathcal{A}_1 T^2 \exp\left(-\frac{\phi_p + \phi_d}{kT}\right) \left(\exp(V_1/V_t) - 1\right), \tag{14}$$

where A_p^* is the effective Richardson constant associated with thermionic emission of holes, ϕ_p is the Schottky barrier height for holes, and ϕ_d is the diffusion potential given by

$$\phi_d = \phi_n - qV_t \ln(N_C/N_D), \tag{15}$$

where N_C is the conduction band density of states and N_D is the background carrier concentration. Note that the sum of the Schottky barrier height for electrons and holes is equal to the band gap of the semiconductor. In the limit of large bias voltages ($V_b \gg V_t$), the upper bound on the hole dark current becomes

$$I_{p1} \leq A_p^* \mathcal{A}_1 T^2 \exp(-E_g/kT) \left(\frac{N_C}{N_D}\right), \tag{16}$$

where E_g is the energy gap of the semiconductor. Any hole recombination in the device would reduce this current further. When Eqns. (11) and (16) are evaluated numerically for typical GaAs material parameters, it is found that the hole current is many orders of magnitude smaller than the electron current. Under these circumstances, one is justified in neglecting the hole current and in assuming that the device dark current is primarily dominated by the majority carrier dark current for bias voltages less than the reach-through voltage.

For bias voltages greater than the reach-through voltage but less than the flat-band voltage, one can use one-dimensional analysis to obtain an approximate solution to Poisson's equation in the fully depleted region between the electrodes. One can determine from this analysis the extent to which the energy bands bend and the reduction of the effective barrier height from its maximum value of $\phi_p + \phi_d$. Since there is no recombination in the fully depleted device, the dark current due to holes will simply be the thermionically emitted hole current at the forward-biased electrode where the effective barrier height has been reduced and can be determined approximately by a solution of the Poisson equation. The resulting hole dark current is given by

$$I_{p1} = A_p^* \mathcal{A}_1 T^2 \exp(-\phi_p/V_t) \left[\exp\left(\frac{-(V_{FB} - V_b)^2}{4V_{FB}V_t}\right)\right] \tag{17}$$

for bias voltages between the reach-through and flat-band voltages. This expression is identical to one derived by Sze *et al.* [6]. Finally, when the flat-band voltage is reached, the effective barrier height is reduced to the Schottky barrier for holes (ϕ_p) and the dark current due to the holes is simply

$$I_{p1} = J_{sp}\mathcal{A}_1, \tag{18}$$

for

$$V_{FB} < V_b \leq V_{BR} \tag{19}$$

where V_{BR} is the breakdown voltage and J_{sp} is given by

$$J_{sp} = A_p^* T^2 \exp(-\phi_p / V_t). \tag{20}$$

The total dark current is obtained by adding the contributions from the electron and hole currents in the various regions of the bias voltage. Observe that the total dark current saturates for $V_b > V_{RT}$.

As mentioned previously, one minor limitation of the method discussed here for calculating the dark current is that the two break points in the model, the reach-through and flat-band voltage points, cannot be easily determined in closed-form. These points can, however, be evaluated numerically and then used in the model. In comparing detector performance limits, it is usually not necessary to know exactly where the break points are. For the efficient operation of an MSM as a fast photodetector, the device will almost always be operated at a sufficiently large bias point that it is fully depleted and the carriers move at their saturated velocities. The bias point is then, by definition, somewhere above the reach-through voltage and usually well above the flat-band voltage. The figures-of-merit for various device geometries are therefore best evaluated when the devices are operated in this mode.

A rather interesting observation worth pointing out here is that the dark current expressions depend on the total electrode areas of both polarities. In the conventional interdigitated geometry, the areas of opposite polarity are equal. In the concentric electrode geometry, however, they are not. If the areas of the annular electrodes of one polarity are added and compared with the total area for the other polarity, the two values are not the same. Thus, in the concentric electrode devices, one has an extra degree of freedom in minimizing the dark current. This can be done by choosing the electrode polarities such that the set of electrodes with the smaller total area multiply the dominant contributor to the dark current density. This will result in a smaller dark current. This judicious choice of electrode polarity

is not possible in the conventional interdigitated electrode devices. To choose the correct bias voltage polarity, one notes from Eqn. (11) that the majority carrier current (electrons in this case) varies as the area of the reverse biased electrode. The maximum value of the minority carrier current, on the other hand, as can be seen from Eqn. (18), varies with the area of the forward biased electrodes. This current reaches its saturation value only after the device bias voltage has reached the flat-band voltage (or higher).

As can be seen from Fig. 5, the dark current-voltage characteristic computed from the model developed here is in close agreement with that calculated using numerical methods with the full drift-diffusion equations. The only notable discrepancy between the two characteristics is in the transition region between the reach-through and the flat-band voltages, which in our case occurs between 0.75 and 4.0 Volts. This is to be expected because the model is derived from one-dimensional considerations in this region.

2.3.2. Steady-State Optical Response

It was stated in Section 2.2 that all photons not reflected from the top of the active semiconductor layer are absorbed in the depletion region where they suffer negligible recombination. Mathematically, the photocurrent generated due to the absorbed photons can be related to the incident photon thus:

$$I_{ph} \propto q\eta\phi(t), \tag{21}$$

where I_{ph} is the generated steady-state photocurrent, $\phi(t)$ is the photon arrival rate and η the efficiency of conversion of absorbed photons into electron-hole pairs.

The equation for the steady-state current can be developed from Eqns. (1) and (2). In this development, we assume no recombination so that at the steady-state when $\partial n/\partial t = \partial p/\partial t = 0$, the following equations result:

$$\nabla \cdot \mathbf{J}_n = -q(G_{opt} + G_{th}) \tag{22}$$

and

$$\nabla \cdot \mathbf{J}_p = q\left(G_{opt} + G_{th}\right), \tag{23}$$

where G_{opt} and G_{th} are, respectively, the optical and thermal carrier generation rates. Recombination in the depletion layer has been neglected. The currents $\mathbf{J}_n$ and $\mathbf{J}_p$ can be separated into the constituent photocurrent and dark current terms as follows:

$$\mathbf{J}_n = \mathbf{J}_{n_{ph}} + \mathbf{J}_{n_d} \tag{24}$$

and

$$\mathbf{J}_p = \mathbf{J}_{p_{ph}} + \mathbf{J}_{p_d}, \tag{25}$$

where $\mathbf{J}_{n_{ph}}$ and $\mathbf{J}_{p_{ph}}$ are the photocurrent terms and $\mathbf{J}_{n_d}$ and $\mathbf{J}_{p_d}$ are the dark current terms for electrons and holes, respectively. Since these equations are linear, one can extract the relations relevant for the photocurrent as

$$\nabla \cdot \mathbf{J}_{n_{ph}} = -qG_{opt} \tag{26}$$

and

$$\nabla \cdot \mathbf{J}_{p_{ph}} = qG_{opt}. \tag{27}$$

From Gauss' divergence theorem, one obtains

$$\int_{A_{dep}} \mathbf{J}_{n_{ph}} \cdot dA = -q \int_{V_{dep}} G_{opt} dV \tag{28}$$

and

$$\int_{A_{dep}} \mathbf{J}_{p_{ph}} \cdot dA = q \int_{V_{dep}} G_{opt} dV, \tag{29}$$

where A_{dep} and V_{dep} denote the area and volume, respectively, bounding the depletion region.

These equations can be interpreted in a fairly straightforward manner within the framework of our premise. Since any photons not reflected from the surface of the device are

absorbed in the depletion region, the integral on the right hand sides of the equations simply represents the carrier generation rate multiplied by the electronic charge q. This is equivalent to the product of the normal component of the incident optical intensity, the power transmissivity coefficient of the active layer, the total area of the device not covered by electrodes, and the conversion efficiency of photons to electron-hole pairs.

The left-hand side integrals simply represent the photocurrent extracted by each electrode. In this case, the electron photocurrent will be non-zero only at the positive contacts and the hole photocurrent will be non-zero only at the negative contacts. This leads to the following set of equations for the photocurrent:

$$\int_{A_-} \mathbf{J}_{p_{ph}} \cdot dA = -\int_{A_+} \mathbf{J}_{n_{ph}} \cdot dA = \left[\frac{q\eta(1-R)\lambda}{hc}\right] | < \mathbf{S} > |(A_a - A_m), \tag{30}$$

where A_+ and A_- denote the surfaces bounded by the positively and negatively biased electrodes, respectively. A_a is the total active device area, A_m is the metallized area, R is the reflectivity of the active layer at the wavelength λ and $< \mathbf{S} >$ is the time-average Poynting vector of the normal incident optical radiation. The other parameters have their usual meanings and for future reference, we shall define $\phi_0 \equiv [\eta(1-R)\lambda < \mathbf{S} >]/hc$. Note that the electron and hole photocurrents are equal in magnitude. The steady-state photocurrent is then

$$I_{ph} = \left[\frac{q\eta\,(1-R)\,\lambda}{hc}\right] | < \mathbf{S} > |(A_a - A_m). \tag{31}$$

2.3.3. Capacitance

The effective capacitance of the conventional interdigitated MSM structures can be calculated using conformal mapping techniques when the depletion capacitance is neglected and two-dimensional analysis is used for a pair of electrodes. The resulting expression for the effective capacitance is given by[7]

$$C = N_t \epsilon_0 (1 + \epsilon_r) \frac{K(k)}{K'(k')}, \tag{32}$$

where N_t is the total number of gaps in the interdigitated structure, ϵ_r is the relative dielectric constant of the material, $K(k)$ and $K'(k')$ both denote the complete elliptic integrals of the first kind, $k = \tan^2(4a/\pi b)$, and $k' = \sqrt{1 - k^2}$.

For the concentric electrode structure, however, the analysis is not so simple. Consider, for example, the Laplace equation for the potential in both Cartesian and cylindrical coordinate systems:

$$\frac{\partial^2 \varphi}{\partial z^2} + \frac{\partial^2 \varphi}{\partial x^2} + \frac{\partial^2 \varphi}{\partial y^2} = 0 \tag{33}$$

and

$$\frac{\partial^2 \varphi}{\partial z^2} + \frac{\partial^2 \varphi}{\partial r^2} + \frac{1}{r}\frac{\partial \varphi}{\partial r} = 0. \tag{34}$$

In the cylindrical coordinate system, the Laplace equation has the term $\partial\varphi/r\partial r$ which breaks the symmetry of the device from one electrode period to another. Conformal mapping techniques cannot be applied to this equation because a single pair of electrodes cannot be considered in isolation. In any case, conformal mapping techniques are only useful when the Laplace equation has the exact form of Eqn. (33) [11]. Closed form expressions for the capacitance of the concentric electrode detector are not, therefore, as obvious as those for the conventional device. We have therefore chosen to use a numerical solution of the Laplace equation in cylindrical coordinates for the potential and the associated field relations to obtain the capacitance. In this formulation, we use a standard finite-difference rendition of the Laplace equation, including Dirichlet conditions on the electrodes and the no-flux conditions on the rest of the boundary. The resulting equations are given below.

$$\frac{\varphi_{i+1,j}\,(1+\Delta r/r_i)+\varphi_{i-1,j}\,(1-\Delta r/r_i)-2\varphi_{i,j}}{\Delta r^2}+\frac{\varphi_{i,j-1}+\varphi_{i,j+1}-2\varphi_{i,j}}{\Delta z^2}\approx 0 \qquad (35)$$

$$\varphi_{i,0}=\frac{V_b}{2} \qquad (36)$$

if $R_{i_k} < r_i < R_{o_k}$ and k is even; or

$$\varphi_{i,0}=\frac{-V_b}{2} \qquad (37)$$

if $R_{i_k} < r_i < R_{o_k}$ and k is odd. Otherwise

$$\varphi_{i,j-1}=\varphi_{i,j+1} \qquad (38)$$

for all other values of r_i when $j = 0$ or N and

$$\varphi_{i+1,j}=\varphi_{i-1,j} \qquad (39)$$

when $i = 0$ or $i = \ell$. In the above set of equations, i is the index for the location of a point on the r axis and is an integer ranging from 0 to ℓ. The index variable j determines the z coordinate of a given point and ranges from 0 to N. Since this method requires a finite domain with respect to both coordinates, z_N and r_ℓ must be chosen to be large enough to ensure that the electric fields have decayed well before these boundaries are reached. In this notation, V_b is the applied bias voltage and k is the index denoting the concentric electrodes, with $k = 0$ corresponding to the central disk and $k = N_e$ corresponding to the outermost annular electrode. R_{o_k} denotes the outer radius of the kth electrode and R_{i_k} denotes the inner radius of the same electrode.

This set of linear equations is solved to give the electrostatic potential using a standard Gauss-Seidel iterative method. The resulting potential solution can then be used to obtain the capacitance symbolically according to

$$C=\frac{Q_t}{16\,V_b} \qquad (40)$$

where

$$Q_t = \int_{A_1} \sigma_s dA = \int_0^{2\pi} \int_{r'} \sigma_s(r) dr d\theta \tag{41}$$

and

$$\sigma_s = \epsilon \mathbf{E}(r,0) \cdot \hat{z} = -\epsilon \frac{\partial \varphi}{\partial z}(r,0); \tag{42}$$

in this presentation, σ_s is the surface charge density on the electrodes, $\hat{z}$ is the unit vector normal to the electrodes, and Q_t is the magnitude of the total charge on the positively biased electrodes. And finally, the working capacitance relation is given as

$$C = \left[\frac{2\pi(1+\epsilon_r)\epsilon_0 \Delta r}{V_b \Delta z}\right] \sum (\varphi_{i',0} - \varphi_{i',1}) r_{i'}. \tag{43}$$

where the subscript i' indicates summation over the positive electrodes. This technique requires a modest amount of computational effort. It is still, however, faster to implement than the complete drift-diffusion equations.

2.3.4. The Intrinsic Frequency Response of MSM Photodetectors

2.3.5. Conventional Interdigitated Electrode Geometry

A simple frequency response function for an MSM detector can be derived if one assumes that the photogenerated carriers travel at their saturated velocities across the depletion layer. For this derivation, consider the rectangular pair of electrodes shown in Fig. 6. A thin sheet of electron-hole pairs is photogenrated at some position x' between the electrodes. Let the electron-hole pair photogeneration be caused by a modulated light source described by

$$\phi(t) = \phi_0 \exp(j\omega t) \tag{44}$$

where ϕ_0 is as defined previously and ω is the modulation frequency. The time required for an electron generated at position x' and collected at the positively biased electrode is $\tau_e' = x'/v_{se}$. The corresponding time for a hole liberated at the same position and collected

at the negatively biased electrode is $\tau_h' = (W - x')/v_{sh}$. The parameters v_{se} and v_{sh} are, respectively, the electron and the hole saturation velocities.

It can be shown that the current impulse observed in a external circuit resulting from a single electron generated at the position x' as shown in Fig. 6 is

$$\delta i_e = \frac{qv(t)}{W} \tag{45}$$

where q is the electronic charge and $v(t)$ is the instantaneous electron velocity—-which in this case is the saturated velocity, v_{se}. The corresponding current impulse due to a hole is

$$\delta i_h = \frac{qv(t)}{W} = \frac{qv_{sh}}{W}. \tag{46}$$

From these simple arguments, it follows that the instantaneous photocurrent due to the electron-hole pairs generated at time t is

$$J_{ph}(t) = \int_{t-\tau_e'}^{t} \frac{qv_{se}\phi_0 \exp(j\omega t')}{W} dt' + \int_{t-\tau_h'}^{t} \frac{qv_{sh}\phi_0 \exp(j\omega t')}{W} dt'. \tag{47}$$

Note that since a carrier spends a time $\tau_{e(h)}'$ in transit, the instantaneous current at some arbitrary time t is the sum of the current contributions from carriers generated between the times t and $t - \tau_{e(h)}'$. The instantaneous photocurrent expression in Eqn. (47) evaluates to

$$J_{ph} = q\phi_0 e^{j\omega t}\left[\frac{1 - \exp(-j\omega(x'/v_{se})}{j\omega\tau_e} + \frac{1 - \exp(-j\omega(W - x')/v_{sh})}{j\omega\tau_h}\right] \tag{48}$$

where we have substituted x'/v_{se} for τ_e' and $(W - x')/v_{sh}$ for τ_h' and defined the electron (hole) transit time between the electrodes as

$$\tau_{e(h)} = \frac{W}{v_{se(h)}}. \tag{49}$$

The total photocurrent generated by a single MSM device which consists of a pair of electrodes of length L and separated by a width W is given by the expression

$$I_{ph}(t) = \int_0^L \int_0^W q\phi_0 e^{j\omega t}\left[\frac{1 - \exp[-j\omega(x'/v_{se})]}{j\omega\tau_e} + \frac{1 - \exp[-j\omega(W - x'/v_{sh})]}{j\omega\tau_h}\right] dx'dy'. \tag{50}$$

This evaluates to

$$I_{ph}(t) = q\phi_0 LW e^{j\omega t}\left[\frac{j\omega\tau_e + e^{-j\omega\tau_e} - 1}{(j\omega\tau_e)^2} + \frac{j\omega\tau_h + e^{-j\omega\tau_h} - 1}{(j\omega\tau_h)^2}\right]. \tag{51}$$

Using the definition for ϕ_0 from our previous discussion of the steady-state optical response, the photocurrent can be rewritten in terms of the incident optical power P_{in} as

$$I_{ph}(t) = \left[\frac{q\eta(1-R)\lambda}{hc}\right] P_{in} e^{j\omega t} H(\omega). \tag{52}$$

The factor

$$H(\omega) = \left[\frac{j\omega\tau_e + e^{-j\omega\tau_e} - 1}{(j\omega\tau_e)^2} + \frac{j\omega\tau_h + e^{-j\omega\tau_h} - 1}{(j\omega\tau_h)^2}\right] \tag{53}$$

represents the carrier transit-time limited response of a single MSM device. This is also the response of any interdigitated electrode MSM device with an arbitrary number of electrode pairs. We call this response the *intrinsic* frequency response to distinguish it from the function which obtains when the device is connected to an external circuit. The 3 dB bandwidth of conventional MSM devices can be estimated from the $|H(\omega)|$ function. This function is plotted in Fig. 7 for a typical device fabricated from GaAs material. The bandwidth is about 37 GHz.

2.3.6. New Concentric Electrode Geometry

The frequency response of the concentric electrode devices can be derived in a manner analogous to the interdigitated case. We consider the concentric electrode device shown in Fig. 2. The photocurrent generated within the first annular gap bounded by the positively biased central disk and the first negatively biased concentric electrode is given by the expression

$$I_{ph}(t) = \int_0^{2\pi}\int_{R_o^+}^{R_i^-} q\phi_0 e^{j\omega t}\left[\frac{1-\exp\left[-j\omega(r-R_o^+)/v_{se}\right]}{j\omega\tau_e} + \frac{1-\exp\left[-j\omega(R_i^- - r)/v_{sh}\right]}{j\omega\tau_h}\right] r\,dr\,d\theta \tag{54}$$

where R_o^+ is the outer radius of the positively biased electrode and R_i^- is the inner radius of the negatively biased electrode. This expression evaluates to

$$I_{ph}(t) = q\phi_0 e^{j\omega t}\pi \left([R_i^-]^2 - [R_o^+]^2\right) H_{c\uparrow}(\omega) \tag{55}$$

where

$$H_{c\uparrow}(\omega) = H_{1\uparrow}(\omega) + H_{2\uparrow}(\omega) + H_{3\uparrow}(\omega), \tag{56}$$

and

$$H_{1\uparrow}(\omega) = \left[\frac{1}{j\omega\tau_e} + \frac{1}{j\omega\tau_h}\right], \tag{57}$$

$$H_{2\uparrow}(\omega) = \left[\frac{2W_c}{[R_i^-]^2 - [R_o^+]^2}\right]\left[\frac{R_i^- e^{-j\omega\tau_e} - R_o^+}{(j\omega\tau_e)^2} + \frac{R_o^+ e^{-j\omega\tau_h} - R_i^-}{(j\omega\tau_h)^2}\right] \tag{58}$$

and

$$H_{3\uparrow}(\omega) = \left[\frac{2W_c^2}{[R_i^-]^2 - [R_o^+]^2}\right]\left[\frac{e^{-j\omega\tau_e} - 1}{(j\omega\tau_e)^3} - \frac{e^{-j\omega\tau_h} - 1}{(j\omega\tau_h)^3}\right]. \tag{59}$$

Note that in the concentric electrode case, we have made the following definitions, $W_c \equiv R_i^- - R_o^+$ and $\tau_{e(h)} \equiv W_c/v_{se(h)}$.

The expression for the photocurrent for the second annular gap, which is bounded by a negatively biased electrode in the inner radius and a positively biased electrode on the outer radius, can be shown to be

$$I_{ph}(t) = q\phi_0 e^{j\omega t}\pi \left([R_i^+]^2 - [R_o^-]^2\right) H_{c\downarrow}(\omega) \tag{60}$$

where

$$H_{c\downarrow}(\omega) = H_{1\downarrow}(\omega) \pm H_{2\downarrow}(\omega) + H_{3\downarrow}(\omega), \tag{61}$$

and

$$H_{1\downarrow}(\omega) = \left[\frac{1}{j\omega\tau_e} + \frac{1}{j\omega\tau_h}\right], \tag{62}$$

$$H_{2\downarrow}(\omega) = \left[\frac{2W_c}{[R_i^+]^2 - [R_o^-]^2}\right]\left[\frac{R_i^+ e^{-j\omega\tau_h} - R_o^-}{(j\omega\tau_h)^2} + \frac{R_o^- e^{-j\omega\tau_e} - R_i^+}{(j\omega\tau_e)^2}\right] \tag{63}$$

and

$$H_{3\downarrow}(\omega) = \left[\frac{2W_c^2}{[R_i^+]^2 - [R_o^-]^2}\right]\left[\frac{e^{-j\omega\tau_h} - 1}{(j\omega\tau_h)^3} - \frac{e^{-j\omega\tau_e} - 1}{(j\omega\tau_e)^3}\right]. \tag{64}$$

For a multiple (concentric) electrode MSM device the two expressions for the photocurrent derived above must be generalized to give the total photocurrent over the entire device. It is a fairly straight-forward, but tedious, exercise in algebra to show that the complete photocurrent expression for N_e electrodes is

$$I_{ph}(t) = q\phi_0 e^{j\omega t}\pi R^2 H_c(\omega). \tag{65}$$

The function $H_c(\omega)$ is defined thus:

$$H_c(\omega) = H_1(\omega) + H_2(\omega) + H_3(\omega), \tag{66}$$

where

$$H_1(\omega) = \left[\frac{1}{j\omega\tau_e} + \frac{1}{j\omega\tau_h}\right], \tag{67}$$

$$H_2(\omega) = \frac{2W_c}{R^2}\left[\frac{\rho^- e^{-j\omega\tau_e} - \varrho^+}{(j\omega\tau_e)^2} + \frac{\varrho^+ e^{-j\omega\tau_h} - \rho^-}{(j\omega\tau_h)^2}\right], \tag{68}$$

and

$$H_3(\omega) = \frac{W_c^2}{R^2}\left[1 - (-1)^{N_e}\right]\left[\frac{e^{-j\omega\tau_e} - 1}{(j\omega\tau_e)^3} - \frac{e^{-j\omega\tau_h} - 1}{(j\omega\tau_h)^3}\right]. \tag{69}$$

We have also made the following additional variable definitions:

$$\rho^{-} = \sum_{k=0}^{M} R^{-}_{i(2k+1)} + \sum_{k=0}^{M'} R^{-}_{o(2k+1)}, \tag{70}$$

$$\varrho^{+} = \sum_{k=0}^{M} R^{+}_{o2k} + \sum_{k=0}^{M'} R^{+}_{i(2k+2)}, \tag{71}$$

$$R^2 = \sum_{k=0}^{N_e-1} \left[[R_{i(k+1)}]^2 - [R_{ok}]^2 \right], \tag{72}$$

where $M = (N_e - 1)/2$ for N_e odd or $M = N_e/2$ for N_e even and $M' = M$ for even N_e or $M' = M - 1$ for N_e odd.

In the derivation of the expressions above, we have assumed that the central disk of the device is positively biased. Subsequent electrodes, therefore, take on alternating negative and positive polarities. If the central disk had been biased negatively, then the photocurrent expressions would have been slightly different; the differences being attributed to the sign of the carriers and the new direction in which they are now being transported. The fundamental physics of the device, however, remains the same, and in fact, the device Bode plot is exactly identical to that shown in Fig. 7 for a device whose central disk is positively biased.

3. Comparison of Important Performance Characteristics

The theoretical framework discussed in this paper can be used to compare some of the key operating characteristics of MSM photodetectors in both the conventional interdigitated and the new concentric electrode geometry. The methods developed within the framework can also be used to identify guidelines for optimal feature size dimensions and configuration.

There are several ways to specify device feature sizes: one way is to specify the ratio of the total metalized device area to the total device area. We call this ratio the *fill ratio.* For the conventional interdigitated electrode devices, we must specify the electrode width, a, and the inter-electrode spacing, b, in addition to the number of desired electrode pairs. For the concentric electrode devices, one must also specify the radius of the central disk, R_c.

For purely illustrative purposes, we have chosen to compare MSM devices from both geometries with nominally the same active areas. The results discussed here are based on a concentric electrode device with a device radius of 25 μm. The dimensions of the conventional interdigitated device are then chosen to corresond to an area of the same size as that of the concentric device. The parameter of most interest when designing MSM photodectors is usually the *external* frequency response. This response is the compounded response of the device as computed from carrier transit time limitations and the response controlled by the overall capacitive and inductive effects of the device geometry. The capacitive and inductive effects are very difficult to quantify since they usually depend on the details of the fabrication process in addition to the measurement techniques employed.

3.1. Intrinsic Frequency Response Characteristics

A theoretical comparison of the *intrinsic* frequency response for the two device geometries for identical nominal active areas and feature sizes, yields no significant differences. The frequency responses are calculated using the relations derived in subsections 2.3.5 and 2.3.6. The fact that there is no difference in the *intrinsic* frequency responses for the two geometries is not surprising at all. This is simply because the intrinsic behavior depends on the fundamental physics of the device material and not on the geometrical structure. And in fact, this lends support to the theoretical soundness of the two methods used in computing the *intrinsic* frequency response.

We have also calculated the 3 dB bandwidth of the devices discussed here as a function of the active area gap-width between the electrodes. This information is displayed graphically in Fig. 8. This curve is valid for the intrinsic 3 dB bandwidth for both the interdigitated and concentric electrode devices. The natural trend of increasing bandwidth with decreasing gap-width is clearly evident here. The bandwidths predicted from this graph are in reasonable agreement with the general trends in the literature [8, 9, 10]. The comparison with experimental values should not be pushed too far because the measured values are generally for the *extrinsic* frequency bandwidth which is limited by some the factors mentioned previously.

3.2. Dominant Device Capacitance

The capacitance of the MSM devices is one of the parameters which depends on the particular geometry chosen. We show in Fig. 9 the calculated capacitance values for the two device geometries discussed above for varying values of the *fill ratio*. The techniques used to compute the capacitance values have already been discussed in subsection 2.3.3. In general, the effective capacitance increases as more and more of the active device area is covered with the electrode metallization. This is true for both device geometries. Observe, however, that the capacitance value for a given *fill ratio* is lower for a concentric electrode MSM device than for an interdigitated device. This can be easily understood by considering the equipotential plot shown in Fig. 10. This plot, typical for the devices in the concentric electrode geometry, has one distinguishing feature, that is: the equipotential contours are spaced further apart compared to those for an interdigitated electrode device. Note, for instance, the equipotentials at the central disk. These equipotentials correspond to lower electric field strengths at the electrodes; which in turn, implies a lower charge density, specially at the central disk. In the intergiditated electrode device, the charge is uniformly distributed from

one electrode pair to another. The anomaly in the geometry dependence of the capacitance for the concentric electrode device provides one with a unique option. One can deliberately minimize the device capacitance by optimally choosing the size of the central disk. This is a very significant development since in practical MSM devices, the measured frequency response always depends on the interaction of the effective device capacitance and any external resistive loads.

4. Summary

We have proposed a new geometry for MSM photodetectors and established a framework for the analysis of the performance limits for both the new and the conventional geometry. Although the methods of analysis developed here are fairly elementary, the results they yield agree quite well with those computed using the fully-coupled drift-diffusion equations.

A theoretical comparison of the important device characteristics shows that the concentric electrode device has some important inherent advantages. These advantages ought to make the new device more attractive in practical implementation of the MSM concept.

Finally, we point out that MSM photodetectors suffer from another problem which also limits their performance. This problem is inductance. It is most commonly paid short shrift in the literature. We believe we have a technique which will allow us to almost eliminate this problem in the device geometry proposed here. The methods of analysis of the virtually inductance-free device will be reported elsewhere.

5. Acknowledgment

This work was supported by NSF through a National Science Foundation Young Investigator Award to E. Towe and by NASA Langley Research Center.

References

[1] Y. Liu, W. Khalil, P.B. Fischer, S.Y. Chou, T.Y. Hsiang, S. Alexandrou, and R. Sobolewski, "Nanoscale Ultrafast Metal- Semiconductor-Metal Photodetectors", presented at the 50th IEEE Device Research Conference, MIT, Cambridge, MA, June 22-24,1992.

[2] S.Y. Chou, Y. Liu, and P.B. Fischer, "Tera-hertz GaAs metal-semiconductor-metal photodetectors with 25 nm finger spacing and finger width", *Appl. Phys. Lett.*, vol. 61, pp. 477-479, 1992.

[3] J.B.D. Soole and H. Schumacher, "Transit-Time Limited Frequency Response of InGaAs MSM Photodetectors", *IEEE Trans. Electron Devices.*, vol. ED-37, no. 11, pp. 2285-2291, 1990.

[4] M. Shur, *Physics of Semiconductor Devices*, Englewood-Cliffs, New Jersey: Prentice Hall, 1990, chapter 2.

[5] B.J. Van Zeghbroeck, W. Patrick, J-M. Halbout, and P. Vettiger, "105-GHz Bandwidth Metal-Semiconductor-Metal Photodiode", *IEEE Electorn Device Lett.*, vol. EDL-9, no. 10, pp. 527-529, 1988.

[6] S.M. Sze, D.J. Coleman, Jr., and A. Loya, "Current Transport in Metal-Semiconductor-Metal (MSM) Structures", *Solid State Electronics*, vol. 14, no. 12-C, pp. 1209-1218, 1971.

[7] Y.C. Lim and R.A. Moore, "Properties of Alternately Charged Coplanar Parallel Strips by Conformal Mappings", *IEEE Trans. Electron Devices*, vol. ED-15, no. 3, pp. 173-180, 1968.

[8] O. Wada, H. Nobuhara, H. Hamaguchi, T. Mikawa, A. Tackeuchi, and T. Fuji, "Very high speed GaInAs metal- semiconductor-metal photodiode incorporating an AlInAs/GaInAs graded superlattice", *Appl. Phys. Lett.*, vol. 54, no. 1 pp. 16-17, 1988.

[9] J.F. Vinchant, J.P. Vilcot, J.L. Lorriaux, and D. Decoster, "Monolithic Integration of a thin and short Metal-Semiconductor-Metal Photodetector with a GaAlAs Optical Inverted Rib Waveguide on a GaAs Semi-Insulating Substrate", *Appl. Phys. Lett.*, vol. 55, no. 19, pp. 1966-1968, 1989.

[10] A. N. M. M. Chodhury, C. Jagannath, A. Negri, B. Elman, and C.A. Armineto, "Thermally Stable, Superlattice-Enhanced 1.3 μm InGaAs MSM Photodetectors on GaAs Substrates", *IEEE Electron Device Lett.*, vol. EDL-12, no. 6, pp. 281-283, 1991.

[11] E.B. Saff and A.D. Snider, *Fundamentals of Complex Analysis for Mathematics, Engineering, and Science.* Englewood-Cliffs, New Jersey: Prentice Hall, 1976, chapter 7.

Figure Caption

Fig. 1. Conventional interdigitated electrode MSM photodetector geometry.

Fig. 2. Concentric electrode MSM photodetector geometry.

Fig. 3. Cross section of the concentric electrode MSM photodetector structure.

Fig. 4. Dark current vectors in an MSM photodetector.

Fig. 5. Comparison between simplified dark current model and numeric solution of drift-diffusion equations.

Fig. 6 Geometry used in derivation of MSM frequency response.

Fig. 7 Calculated frequency response of typical GaAs MSM photodetector (1.4 μm gap width).

Fig. 8 Plot of calculated MSM photodetector bandwidth as a function of gap width.

Fig. 9 Capacitance comparison between interdigitated and concentric electrode MSM structures.

Fig. 10 Equipotential contour plots for the concentric MSM device structure.

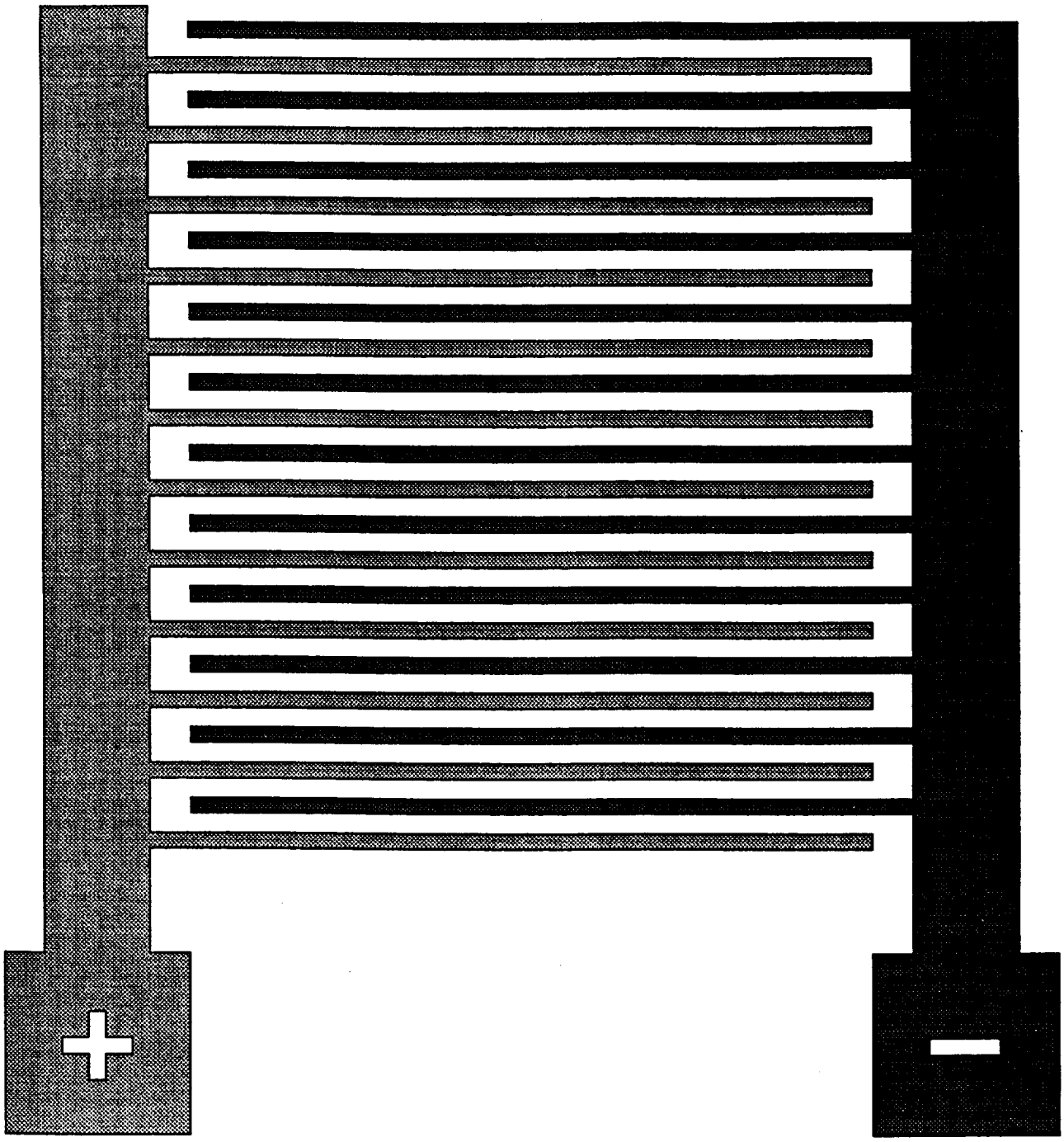

Figure 1

g2725 figure 1 5/93 Towe

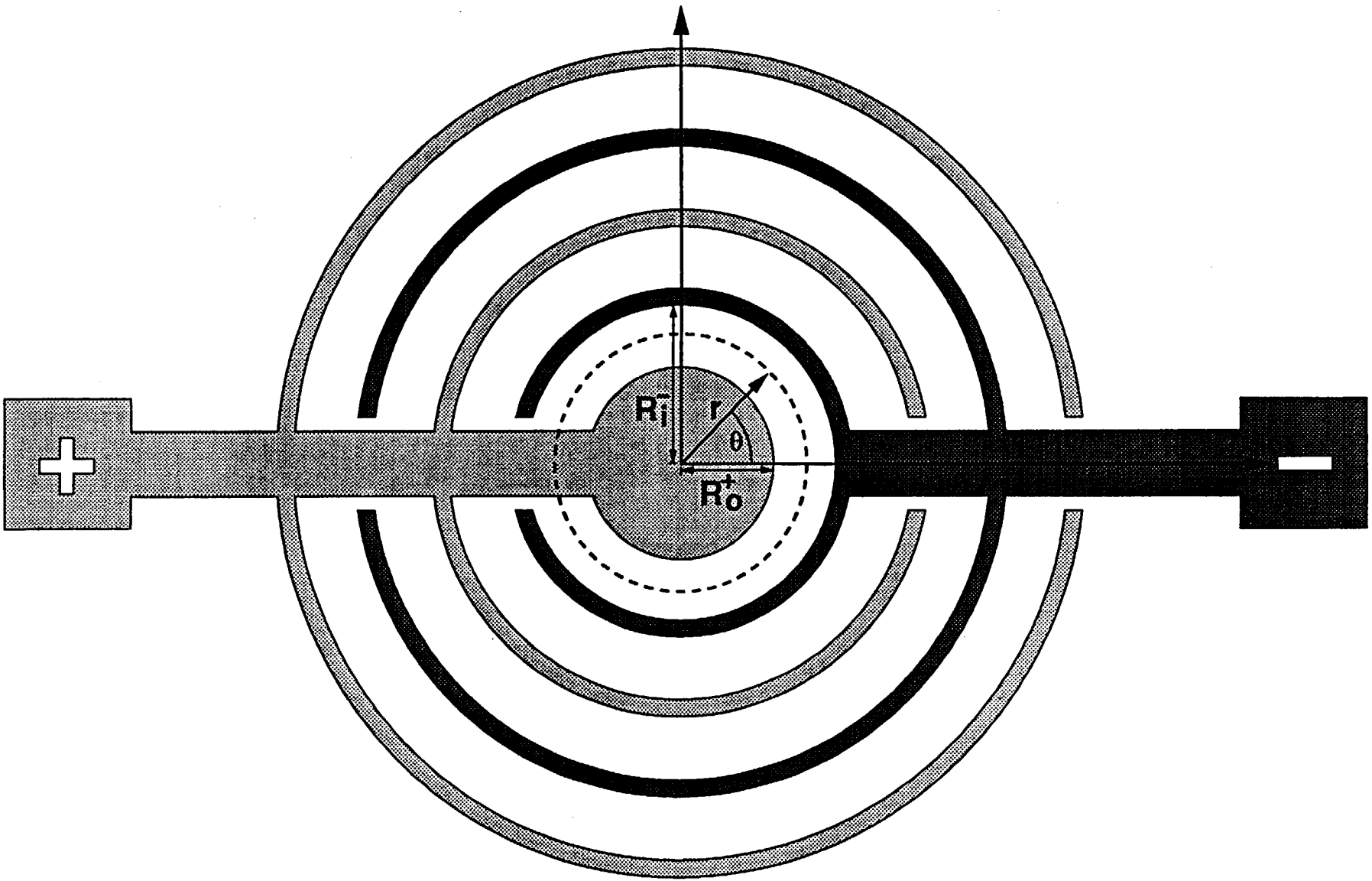

Figure 2

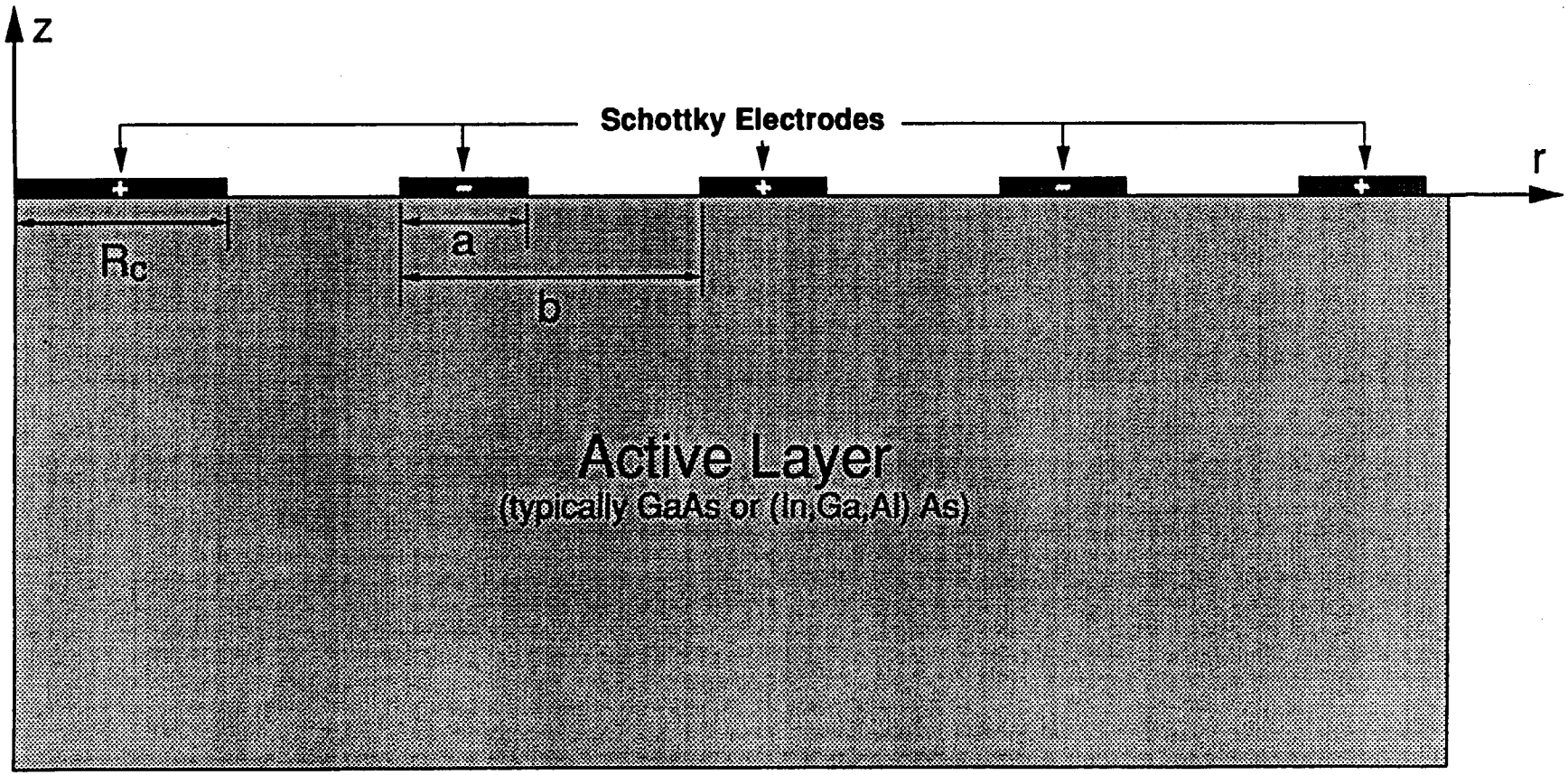

Figure 3

g2725 figure 3 5/93 Towe

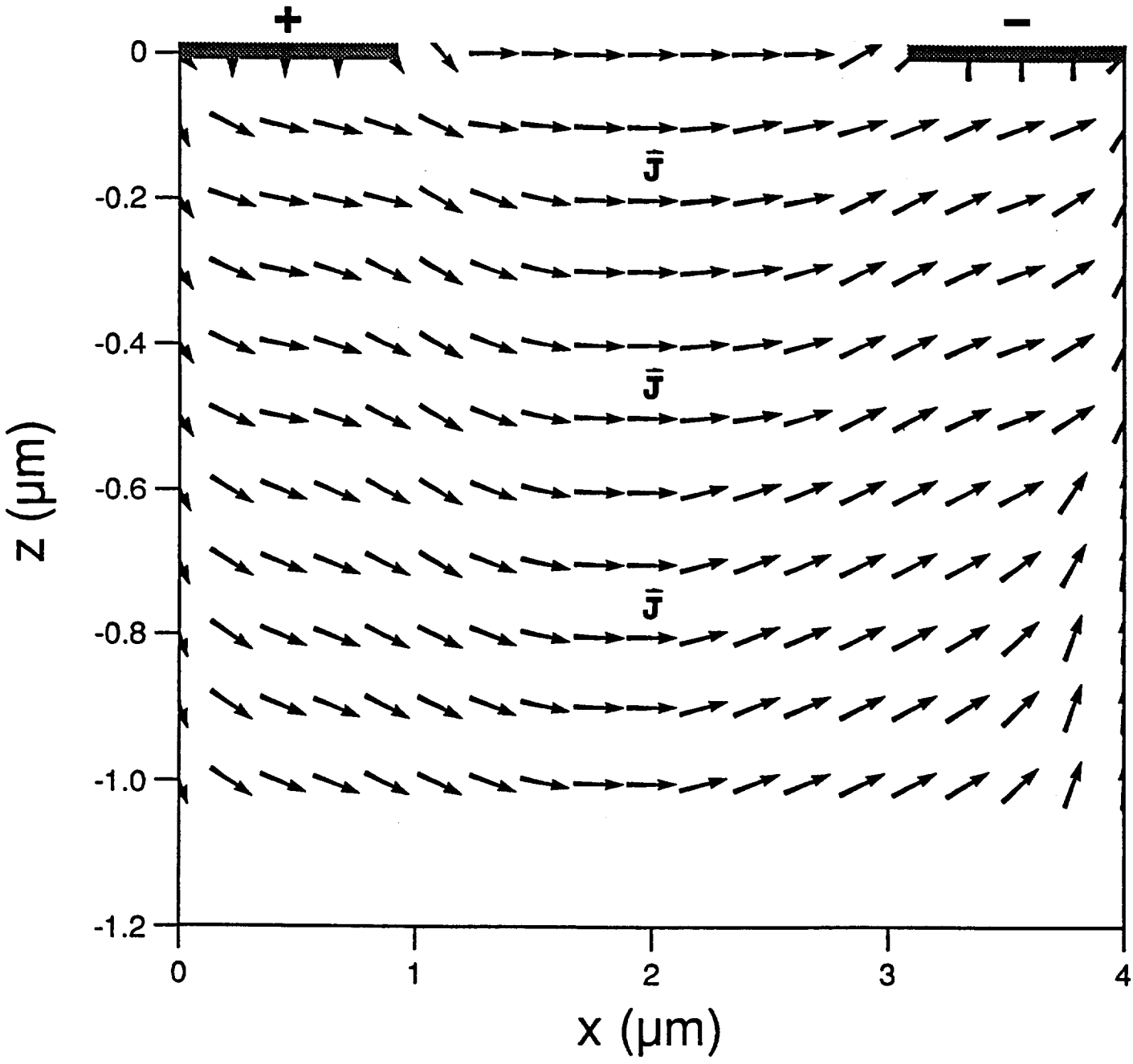

Figure 4

g2725 figure 4 5/93 Towe

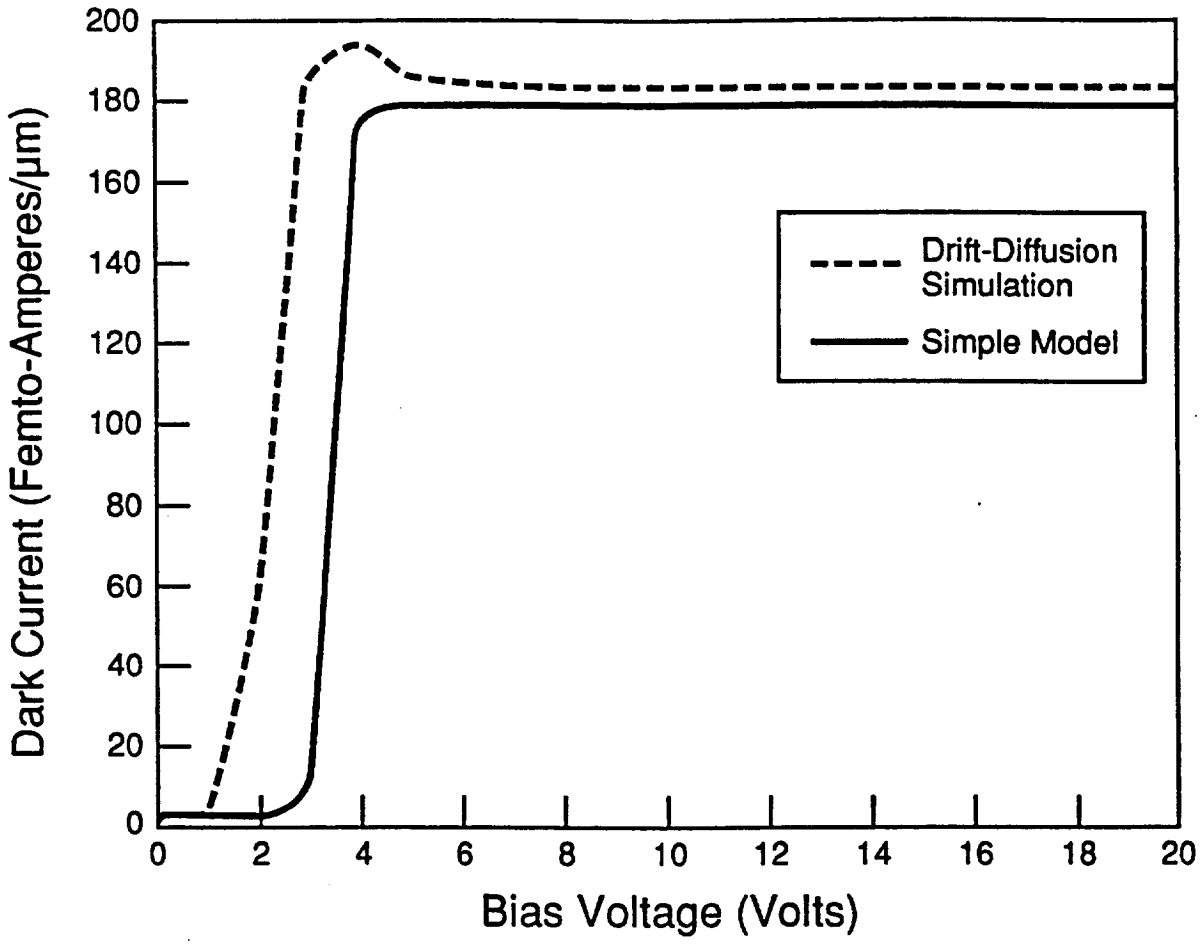

Figure 5

g2725 figure 5 5/93 Towe

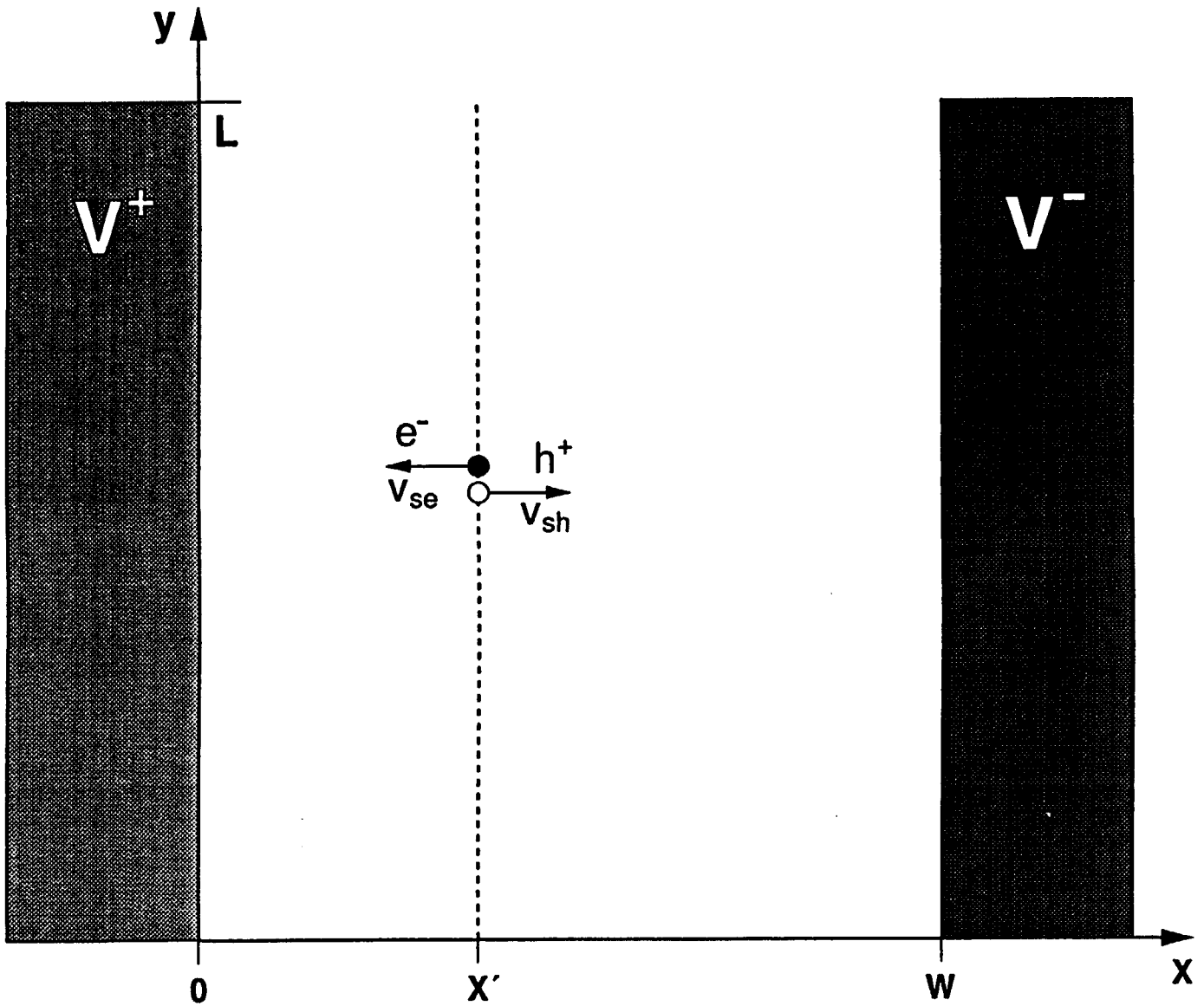

Figure 6

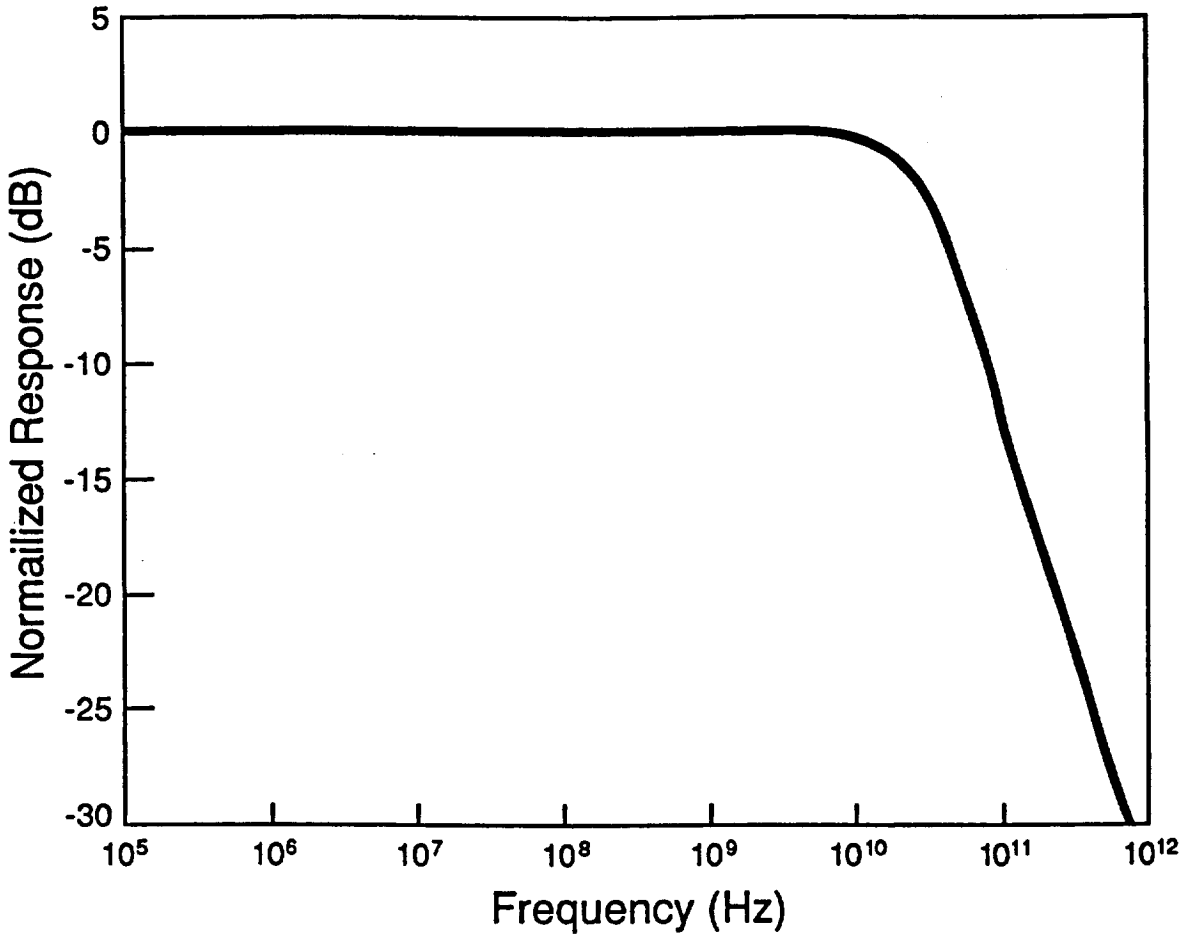

g2725 figure 7 5/93 Towe

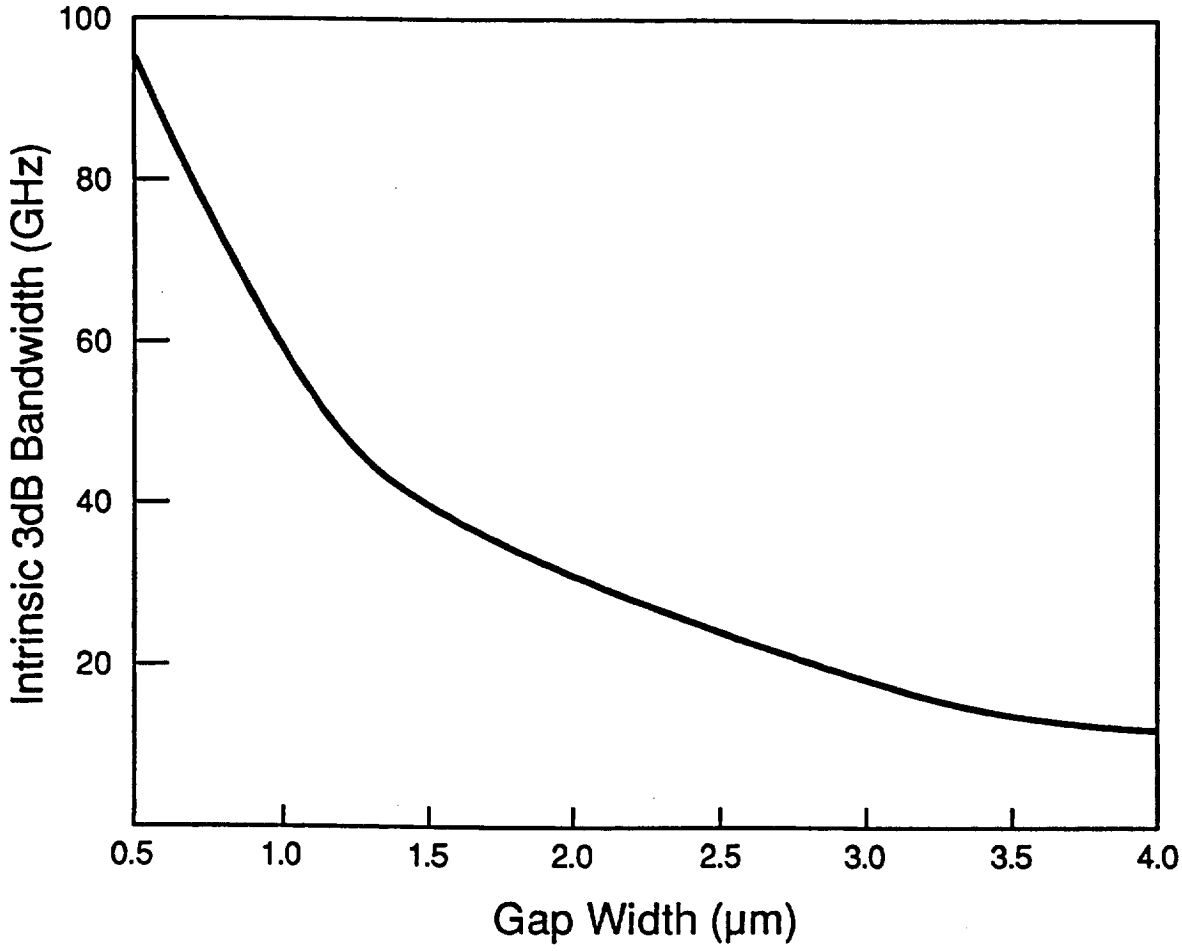
100
80
60
40
20
Intrinsic 3dB Bandwidth (GHz)
0.5
1.0
1.5
2.0
2.5
3.0
3.5
4.0
Gap Width (μm)

Figure 8

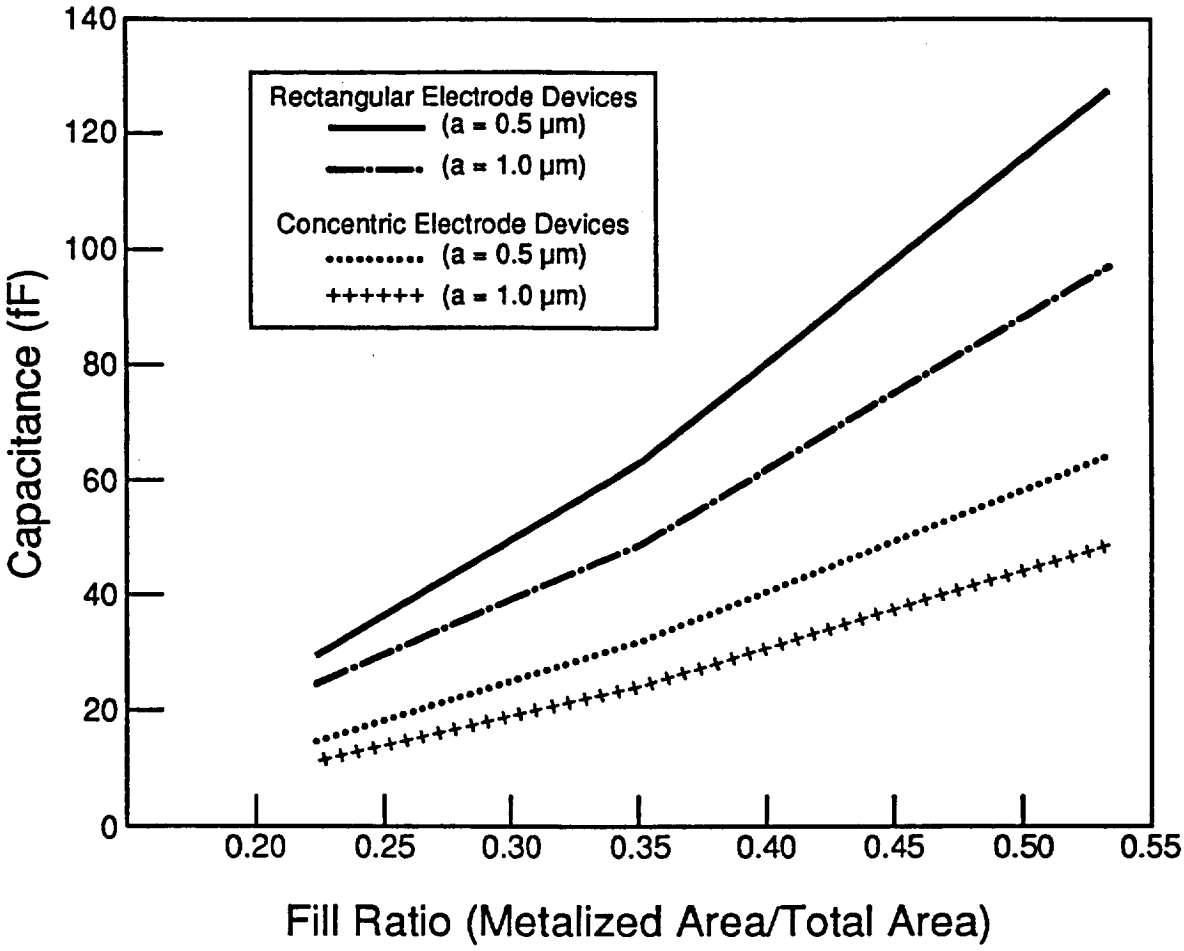

Figure 9

g2725 figure 9 5/93 Towe